RSC Advances

PAPER

View Article Online
View Journal | View Issue

Cite this: *RSC Adv.*, 2018, **8**, 41491

Supported binary CuO_x–Pt catalysts with high activity and thermal stability for the combustion of NH_3 as a carbon-free energy source†

Saaya Kiritoshi,[a] Takeshi Iwasa,[b] Kento Araki,[a] Yusuke Kawabata,[a] Tetsuya Taketsugu,[b] Satoshi Hinokuma*[ac] and Masato Machida[a]

Received 25th September 2018
Accepted 27th November 2018

DOI: 10.1039/c8ra07969b

rsc.li/rsc-advances

Recently, NH_3 has been thought to be a renewable and carbon-free energy source. The use of NH_3 fuel, however, is hindered by its high ignition temperature and N_2O/NO production. To overcome these issues, in this study, the combustion of NH_3 over copper oxide (CuO_x) and platinum (Pt) catalysts supported on aluminium silicates ($3Al_2O_3{\cdot}2SiO_2$), aluminium oxides (Al_2O_3), and silicon oxides (SiO_2) were compared. To achieve high catalytic activity for the combustion of NH_3 and high selectivity for N_2 (or low selectively for N_2O/NO), conditions for the preparation of impregnated binary catalysts were optimised. With respect to the binary catalysts, sequentially impregnated CuO_x/Pt/Al_2O_3 exhibited relatively higher activity, N_2 selectivity, and thermal stability. From XRD and XAFS analyses, CuO_x and Pt in CuO_x/Pt/Al_2O_3 were present as $CuAl_2O_4$ and metallic Pt, respectively. Given that the combustion activity was closely associated with the Pt nanoparticle size, which was estimated from the Scherrer equation and the pulsed CO technique, highly dispersed Pt nanoparticles were crucial for the low-temperature light-off of NH_3. For single and binary catalysts, although NH (imide) deformation modes as a key species for N_2O production were detected by *in situ* FTIR spectral analysis, the band intensity of CuO_x/Pt/Al_2O_3 was less than those of CuO_x/Al_2O_3 and Pt/Al_2O_3. Therefore, CuO_x/Pt/Al_2O_3 exhibits high selectivity for N_2 in NH_3 combustion.

Introduction

Recent studies have reportedly considered NH_3 to serve not only as a H_2 carrier material but also as a renewable, carbon-free energy source because of its high energy density (3160 W h L^{-1}) and negligible thermal NO_x emission.[1] Currently, NH_3 is industrially produced at a high pressure using N_2 (produced from air) and H_2 (produced from natural gas) by employing the Haber–Bosch process, which consumes a large amount of energy. However, the energy and costs associated with H_2 production and natural gas is 70–90% of that required for NH_3 production.[2] Therefore, the low energy and costs that are associated with H_2 production along with the fact that it is a renewable energy source should be emphasised to ensure that the society utilises H_2 along with NH_3. As a proof-of-concept for using NH_3 as a fuel, an NH_3-fuelled micro-gas turbine has been employed to demonstrate the potential of NH_3-fired power plants at the Fukushima Renewable Energy Institute in Japan, as well as an NH_3-fuelled industrial furnace.[3] Compared to fossil fuels, however, NH_3 exhibits disadvantages of a high ignition temperature, low combustion rate, and N_2O/NO_x production. Therefore, to overcome these issues, it is imperative to develop a novel NH_3 combustion system. First, a catalytic NH_3 combustion system, which decreases the ignition temperature and N_2O/NO_x emissions, was developed. Previously, our group has successfully developed a catalytic NH_3 combustion system and novel catalysts exhibiting high activity, N_2 selectivity, and thermal stability.[4] For example, copper oxides (CuO_x) supported on Al_2O_3-based composite oxide materials (such as $10Al_2O_3{\cdot}2B_2O_3$ and $3Al_2O_3{\cdot}2SiO_2$) exhibit high N_2 selectivity and thermal stability, whereas binary CuO_x and silver (Ag) supported on Al_2O_3 exhibit high activity and N_2 selectivity.[4] However, the former catalyst exhibits a low activity (ignition temperature at ~300 °C), while the latter catalyst exhibits low thermal stability (deactivation temperature at ~900 °C likely because of the low melting point of Ag).[4] Therefore, it is imperative to develop catalysts to exhibit high activities and thermal stabilities for NH_3 combustion.

---

[a] *Field of Environmental Chemistry and Materials, Division of Materials Science and Chemistry, Faculty of Advanced Science and Technology, Kumamoto University, 2-39-1 Kurokami, Chuo-ku, Kumamoto 860-8555, Japan. E-mail: hinokuma@kumamoto-u.ac.jp; Tel: +81-96-342-3653*

[b] *Department of Chemistry, Faculty of Science, Hokkaido University, Sapporo 060-0810, Japan*

[c] *International Research Organization for Advanced Science and Technology, Kumamoto University, Japan*

† Electronic supplementary information (ESI) available: Calculation formulae, calculated thermodynamic Pt–PtO_x phase equilibrium, XRD patterns, HAADF-STEM/EDX mapping images, product selectivities for the NH_3–O_2 and NH_3–NO–O_2 reactions, relationship between NH_3 combustion activity and Pt particle size, NH_3- and NO-TPD profiles. See DOI: 10.1039/c8ra07969b

On the other hand, binary systems comprising supported CuO_x–Ag,[5] CuO_x–Pt,[6] CuO_x–Au,[7] CuO_x–CeO_2[8] and –Li_2O_3[8] catalysts exhibiting a high performance for the selective catalytic oxidation of NH_3 (NH_3-SCO) have been previously reported. In particular, CuO_x–Pt systems are expected to exhibit high thermal stability because of the high melting point of Pt (~1770 °C). Recently, Sun *et al.* have synthesised impregnated CuO_x–Pt/ZSM-5 catalysts and reported that CuO_x on Pt species can lead to higher NH_3-SCO performance compared to single catalysts.[6] On the other hand, Jabłońska has synthesised Al_2O_3-, TiO_2-, and ZrO_2-supported CuO_x–Pt, –Pd and –Rh catalysts[6] and found that the supported CuO_x–Pt catalyst exhibits high activity and N_2 selectivity for NH_3-SCO. However, in these studies, NH_3 is considered to cause air pollution; therefore, the thermal stability is investigated at temperatures of less than 900 °C.

In this study, supported binary CuO_x–Pt catalysts were synthesised, and their catalytic properties for the combustion of NH_3 (as an energy source) at high reaction temperatures were examined. To achieve high catalytic activity for the combustion of NH_3, N_2 (low N_2O/NO) selectivity and thermal stability, preparation conditions for impregnated binary catalysts were optimised. Moreover, the relationship between the local structure and catalytic properties for the combustion of NH_3 over supported CuO_x–Pt catalysts was discussed.

Experimental

Catalyst preparation

$3Al_2O_3 \cdot 2SiO_2$ (3A2S) of the catalyst support material was prepared by using an alkoxide method. According to previous studies,[4,9] $Si(OC_2H_5)_4$ (TEOS, Wako Pure Chemicals) was first dissolved in C_2H_5OH (Wako Pure Chemicals) at a concentration of 1 M at room temperature (RT). Second, after the addition of H_2O and HCl (Wako Pure Chemicals), the solution was stirred at 70 °C for 5 h, and a Si solution was prepared. Third, the alcohol was dehydrated. The H_2O and HCl concentrations were H_2O/TEOS $= 2$ (mol mol^{-1}) and HCl/TEOS $= 0.1$ (mol mol^{-1}), respectively. Next, $Al[OCH(CH_3)_2]_3$ (AIP, Sigma-Aldrich) was subjected to reflux conditions and dissolved in $(CH_3)_2CHCH_2OH$ (Nacalai Tesque) to prepare an Al solution. The precursor solution was prepared by mixing the Al and Si solutions in a volume ratio of 3 : 2 at RT. H_2O was added, and the solution was stirred for 1 h to prepare the precursor solution. The precursor sols were dried at 110 °C for 48 h, affording xerogel precursor powders. These powders were pulverised and calcined at 600 °C for 3 h and finally at 1200 °C for 5 h in air. In addition, α-Al_2O_3 (Wako Pure Chemicals), γ-Al_2O_3 (JRC-ALO-8, Catalysis Society of Japan), SiO_2 (JRC-SIO-10, Catalysis Society of Japan), and CuO (Wako Pure Chemicals) were used as support materials.

Single and binary supported CuO_x (CuO loading of 6 wt%) and/or Pt (Pt loading of 2 wt%) catalysts were prepared by the co-impregnation (CuO_x–Pt) of an aqueous solution of $Cu(NO_3)_2$ (Wako Pure Chemicals) and $[Pt(NH_3)_2(NO_3)_2]$ (Tanaka Kikinzoku Kogyo), followed by drying and calcination at 600 °C for 3 h in air. In addition, the sequentially impregnated binary catalysts, *i.e.* Pt and subsequent CuO_x (CuO_x/Pt) and/or CuO_x and subsequent Pt (Pt/CuO_x), were synthesised in a similar fashion. As CuO_x/Pt/Al_2O_3 exhibited a high catalytic activity for the combustion of NH_3, physically mixed catalysts (CuO + Pt/Al_2O_3, $CuAl_2O_4$ + Pt/Al_2O_3, and CuO_x/Al_2O_3 + Pt/Al_2O_3) with the same composition ratios were also prepared. To evaluate their thermal stabilities and catalytic properties, the as-prepared catalysts were subjected to thermal aging at 900 °C for 100 h in air and/or at 1000 °C for 5 h in air.

Characterisation

Powder X-ray diffraction (XRD) patterns were recorded using monochromatic Cu Kα radiation (30 kV, 20 mA, Multiflex, Rigaku). The average size of the Pt particles was calculated by the XRD line broadening method by using the Scherrer equation.[10] The chemical composition was determined by X-ray fluorescence (XRF; EDXL-300, Rigaku) measurements. High-angle annular dark-field scanning transmission electron microscopy (HAADF-STEM) and energy-dispersive X-ray spectroscopy (EDS) mapping images were recorded on a JEM-ARM200CF (JEOL) system. Brunauer–Emmett–Teller (BET) surface area (S_{BET}) values were calculated from the N_2 adsorption isotherms, which were recorded at −196 °C (Belsorp, Bel Japan, Inc.). Pt dispersion and particle size were determined by the pulsed CO technique (BELCAT-B, BEL Japan, Inc.) at 50 °C after O_2 oxidation and subsequent H_2 reduction at 400 °C according to previous studies.[11] Pt dispersion and particle size were calculated by assuming hemispherical particles with the stoichiometric adsorption of CO on Pt at a CO : Pt ratio of 1 : 1. Cu K-edge and Pt L_3-edge X-ray absorption fine structure (XAFS) spectral analyses were carried out at BL9A of PF and BL01B1 of SPring-8. XAFS spectra were recorded in the transmission mode at RT using an ionisation chamber filled with N_2 for the incident beam, another chamber filled with 75% N_2/Ar for the Cu K-edge and 50% N_2/Ar for Pt L_3-edge for the transmitted beam, and a Si(111) double-crystal monochromator. Reference samples (*e.g.* Cu_2O, CuO, $CuAl_2O_4$, and PtO_2) were mixed with boron nitride (BN) powder to achieve an appropriate absorbance at the edge energy, whereas the catalysts were used without mixing with BN. XAFS data were processed using the IFEFFIT software package (Athena and Artemis).

Catalytic NH_3 combustion tests

The catalytic combustion of NH_3 was performed in a flow reactor at atmospheric pressure. Catalysts (10–20 mesh, <0.3 mm thickness, 50 mg) were fixed in a quartz tube (OD: 6 mm, ID: 4 mm) with quartz wool at both ends of the catalyst bed. The temperature dependence of the catalytic activity was evaluated by heating the catalyst bed from RT to 900 °C at a constant rate of 10 °C min^{-1} while a gas mixture containing 1.0% NH_3, 1.5% O_2 and He balance at 100 cm^3 min^{-1} ($W/F = 5.0 \times 10^{-4}$ g min cm^{-3}) was supplied. The O_2 excess ratio for NH_3 combustion was expressed as $\lambda = (pO_2/pNH_3)_{exp.}/(pO_2/pNH_3)_{stoichiom.}$, where p denotes pressure. The NH_3/N_2O/NO, N_2 and NO_2 gas concentrations were analysed using a nondispersive infrared gas analyser (VA-3011, Horiba), chromatography (GC-8A, Shimadzu) and chemiluminescence (NOA-7000, Shimadzu) measurements. The ESI† provides the calculation formulae used to determine the concentration ratios.

In situ Fourier transform infrared (FTIR) spectra were recorded on a Nicolet 6700 spectrometer using a diffuse-reflectance reaction cell with a BaF_2 window connected to a gas supply and a heating system to enable measurements at atmospheric pressure. First, the catalysts were preheated *in situ* in flowing He at 400 °C for 30 min prior to each experiment. After pre-treatment, the temperature of the catalyst was decreased to 200 °C, followed by the subsequent purging of the cell with He and then filling with 0.3% NH_3/He mixed gas. Finally, FTIR spectra were recorded while the catalysts were maintained under a stream of NH_3/He.

Computational details

Spin-restricted density functional theory (DFT) computations were carried out for NH_3/Pt_x ($x = 13$ and/or 20) at the M06 level using the def-SV(P) basis sets, with the 60-electron relativistic effective core potential for Pt, as implemented in TURBOMOLE under the resolution of the identity approximation.[12] The model clusters of Pt_{13} with I_h symmetry and Pt_{20} with T_d symmetry having four (111) faces were locally optimised until imaginary frequencies were removed. One atop geometry for NH_3–Pt_{13} and three initial geometries for NH_3–Pt_{20} were considered, *i.e.* atop the (111) face; bridge-to-edge site; and atop the vertex site, respectively. These geometries were optimised until no imaginary frequencies were observed. The adsorption energy of NH_3 on Pt_x was estimated as $E_{ads} = E(NH_3) + E(Pt_x) - E(NH_3{-}Pt_x)$, where $E(A)$ denotes the electronic energy of species A.

Results & discussion

Local structures of supported CuO_x and Pt catalysts

Fig. 1 shows the XRD patterns of sequentially impregnated binary (CuO_x/Pt) catalysts, because $CuO_x/Pt/Al_2O_3$ exhibited higher activity, N_2 (lower N_2O/NO) selectivity, and thermal stability for the combustion of NH_3 compared to all binary catalysts before and after thermal ageing at 900 °C (Table 1). ESI† shows the XRD patterns of the other catalysts. The XRD patterns of as-prepared CuO_x/Pt/3A2S and $CuO_x/Pt/SiO_2$ before and after aging revealed peaks corresponding to CuO, whereas peaks corresponding to $CuAl_2O_4$ were observed for CuO_x/Pt/3A2S and $CuO_x/Pt/Al_2O_3$ (900 °C), possibly related to the solid-state reaction between γ-Al_2O_3 and CuO_x. Diffraction peaks for Cu species were not observed for as-prepared $CuO_x/Pt/Al_2O_3$, possibly related to the high dispersion of CuO_x. The Al_2O_3 phase for the binary catalysts was transformed from γ to α, and the diffraction peaks for Pt became sharper after thermal aging at temperatures of higher than 900 °C. Therefore, the growth of particles and sintering of Al_2O_3 and Pt are induced by thermal aging. Indeed, the Pt particle sizes calculated by the Scherrer equation increased with the aging temperature (Table 1). On the other hand, as peaks corresponding to CuO were observed for the binary catalysts prepared using α-Al_2O_3 ($CuO_x/Pt/\alpha$-Al_2O_3) before and after aging, it was possibly difficult to form $CuAl_2O_4$ from the solid-state reaction between α-Al_2O_3 and CuO_x (ESI†).

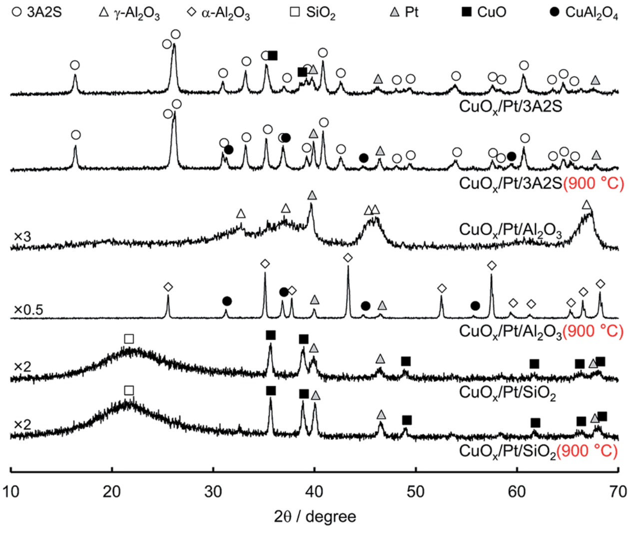

Fig. 1 XRD patterns of sequentially impregnated catalysts before and after thermal aging 900 °C for 100 h in air.

Fig. 2 shows the normalised Cu K-edge X-ray absorption near-edge structure (XANES) spectra and *k*-space extended X-ray absorption fine structure (EXAFS) oscillations of the catalysts and the three reference compounds (Cu_2O, CuO and $CuAl_2O_4$, respectively). Cu K-edge XANES spectra and *k*-space EXAFS oscillations of CuO_x/Pt/3A2S (900 °C) and $CuO_x/Pt/Al_2O_3$ before and after thermal aging at 900 °C were similar to those of $CuAl_2O_4$, whereas those of CuO_x/Pt/3A2S and $CuO_x/Pt/SiO_2$ before and after thermal aging at 900 °C were similar to those of CuO. In the XANES spectra of CuO_x/Pt/3A2S and $CuO_x/Pt/SiO_2$ before and after aging, the pre-edge (at ~8985 eV, corresponding to Cu^{2+} 1s → 4p + ligand and Cu^{2+} 1s → Cu^{2+} charge-transfer excitation)[13] for CuO was observed. XAFS analyses were consistent with the XRD patterns of the catalysts. The Pt L_3-edge XAFS profiles of the catalysts and two references (*i.e.* Pt foil and PtO_2, respectively) are also depicted in Fig. 3. For as-prepared $CuO_x/Pt/Al_2O_3$, the XANES profile was slightly similar to that observed for PtO_2. According to the calculated thermodynamic Pt–PtO_x phase equilibrium (ESI†), PtO_2 and metallic Pt exhibited thermodynamic stability at RT and 600 °C, respectively. Therefore, Pt nanoparticles (especially, their surfaces) in $CuO_x/Pt/Al_2O_3$ are thought to be oxidised during the cooling process of calcination. By contrast, the XANES profiles of the other catalysts were similar to that of Pt foil (metallic Pt) as against the calculated phase equilibrium. This disagreement is supposedly caused by the calcination and/or thermal aging-induced sintering of metallic Pt nanoparticles in these catalysts; hence, the bulk metallic Pt particles are stable at RT.

Next, HAADF-STEM and EDS mapping images of sequentially impregnated $CuO_x/Pt/Al_2O_3$ (900 °C) were recorded (Fig. 4). From the HAADF-STEM image, dispersed nanoparticles with a bright contrast supported on Al_2O_3 particles (blue for Al) were observed, and the EDS mapping images revealed the presence of Pt (red). On the other hand, for the CuO_x species of $CuO_x/Pt/Al_2O_3$ (900 °C), the EDS mapping images revealed the presence of CuO_x aggregates (green). However, because the

Table 1 Catalytic properties of supported catalysts before and after thermal aging at 900 °C for 100 h in air

				Selectivity at T_{90} [a]/%				Pt particle size/nm		Desorbed gas [d]/μmol m^{-2}	
Catalyst	Phase	T_{10} [a]/°C	T_{90} [a]/°C	N_2	N_2O	NO	S_{BET} /m^2 g^{-1}	[b] XRD	[c] Pulsed CO	NH_3	NO
CuO_x/Pt/3A2S	CuO/Pt/3A2S	210	356	90	8	2	32		18		
CuO_x/Pt/3A2S (900 °C)	$CuAl_2O_4$/Pt/3A2S	203	344	89	10	1	27		50		
CuO_x/Al_2O_3	$CuAl_2O_4$/γ-Al_2O_3	303	476	92	6	2	149			1.3	0.050
CuO_x/Al_2O_3 (900 °C)	$CuAl_2O_4$/α, γ-Al_2O_3	295	450	91	8	1	102			0.4	0.063
Pt/Al_2O_3	Pt/γ-Al_2O_3	188	289	81	19	<1	156	11	11	0.6	0.051
Pt/Al_2O_3 (900 °C)	Pt/γ, θ-Al_2O_3	213	266	87	12	<1	99	31	[e] n. d.	2.0	0.140
CuO_x/Pt/Al_2O_3	$CuAl_2O_4$/Pt/γ-Al_2O_3	189	278	86	13	<1	139	15	5	1.6	0.064
CuO_x/Pt/Al_2O_3 (900 °C)	$CuAl_2O_4$/Pt/α-Al_2O_3	220	339	86	13	1	14	33	176	1.5	0.444
CuO_x/Pt/SiO_2	CuO/Pt/SiO_2	234	316	93	7	<1	182	13	[e] n. d.		
CuO_x/Pt/SiO_2 (900 °C)	CuO/Pt/SiO_2	301	456	96	<1	3	81	24	[e] n. d.		

[a] Temperature at which NH_3 conversion reached 10% and 90%. [b] Calculated from XRD line broadening method. [c] Calculated from pulsed CO chemisorption. [d] Estimated by NH_3- and NO-TPD ranging from 50 °C to 500 °C. [e] The amount of CO chemisorption was not detected (n. d.).

overlap of the fluorescence lines of Pt-L and Cu-K, as denoted by the solid arrows in the overlaid image, a physical proximity between Pt and CuO_x nanoparticles in CuO_x/Pt/Al_2O_3 was supposed after aging at 900 °C. On the other hand, Pt particles with sizes larger than 200 nm were clearly observed for CuO_x/Pt/SiO_2 (900 °C) (ESI†).

Combustion properties of supported CuO_x and Pt catalysts

Fig. 5 shows the comparison of the temperature dependence on the selectivities of products obtained over supported CuO_x/Pt, CuO_x/Al_2O_3 and Pt/Al_2O_3 before and after thermal aging at 900 °C under O_2 excess conditions ($\lambda = 2$). ESI† shows those of the other catalysts. With respect to the supported CuO_x/Pt catalysts before and after aging, CuO_x/Pt/Al_2O_3 exhibited a comparatively higher catalytic NH_3 combustion activity and N_2 (lower N_2O/NO) selectivity. For CuO_x/Pt/Al_2O_3 and Pt/Al_2O_3 before and after aging, the light-off curves for NH_3 were obtained at ∼200 °C, whereas CuO_x/Al_2O_3 exhibited lower catalytic activity (T_{10}: ∼300 °C). On the other hand, before and after aging, CuO_x/Pt/Al_2O_3 and CuO_x/Al_2O_3 exhibited lower NO selectivity compared to Pt/Al_2O_3 although NO selectivities for all catalysts were observed after the NH_3 conversion reached ∼90%. In contrast, the selectivity of N_2O over the catalysts before and after aging increased in the order of CuO_x/Al_2O_3 < CuO_x/Pt/Al_2O_3 < Pt/Al_2O_3. Finally, CuO_x/Pt/Al_2O_3 exhibited higher N_2 selectivity. Therefore, binary CuO_x/Pt/Al_2O_3 renders synergistic effects of Pt (enhancing the NH_3–O_2 reaction) and CuO_x (increasing N_2 selectivity). To investigate the low NO selectivity of CuO_x/Pt/Al_2O_3 and CuO_x/Al_2O_3, an NH_3–NO–O_2 reaction test (0.8% NH_3, 0.2% NO, 1.4% O_2, He balance) was also performed (shown in ESI†). For the NH_3–NO reaction, CuO_x/Pt/Al_2O_3 also exhibited higher activity compared to CuO_x/Al_2O_3 and Pt/Al_2O_3. NH_3 was supposedly consumed not only by O_2 but also by NO, which was formed as an intermediate during the light-off of NH_3. However, the selectivity of N_2O for the NH_3–NO–O_2 reaction over CuO_x/Pt/Al_2O_3 was higher than that for the combustion of NH_3 (Fig. 5), indicating that the N_2O is produced from the NH_3–NO reaction.

For N_2O production, on the other hand, according to the kinetic model for NH_3 oxidation, the elementary reaction of NH (imide) + NO → N_2O + H exhibited high sensitivity for N_2O production.[14] Moreover, for catalytic NH_3 oxidation and NH_3–NO reactions, NH was also regarded as a key species for N_2O production.[15] Therefore, to verify the adsorption of NH on the catalysts, *in situ* FTIR spectra of NH_3 adsorbed on the catalysts before and after aging were recorded at 200 °C (Fig. 6); this temperature is the approximate initiation temperature for NH_3 combustion (Fig. 5). As has been reported previously,[15] FTIR bands were observed at 1250 and 1625 cm^{-1}, corresponding to the deformation modes of NH_3 adsorbed on Lewis acid sites, for all catalysts. Moreover, for Pt/Al_2O_3 and CuO_x/Pt/Al_2O_3, a set of bands were slightly observed at 1395 and 1695 cm^{-1}, corresponding to the asymmetric and symmetric bending vibrations of NH_3 species on the Brønsted acid sites. Although the single band at 1458 cm^{-1} corresponding to the NH (considered as a species for N_2O production) deformation modes was observed for all catalysts, the band intensity for CuO_x/Pt/Al_2O_3 was less than that for Pt/Al_2O_3. As CuO_x/Pt/Al_2O_3 prevented the production of NO from the combustion of NH_3 and the dissociative adsorption of NH_3, the catalyst finally achieved high N_2 selectivity.

Catalytic properties of supported CuO_x and/or Pt

Table 1 summarises the catalytic properties of supported CuO_x/Pt, CuO_x/Al_2O_3 and Pt/Al_2O_3 before and after thermal aging at 900 °C, and ESI† shows those of the other catalysts. Catalytic activity was expressed in terms of the light-off temperature at which 10% conversion of NH_3 was achieved (T_{10}), and the product selectivities were evaluated at the reaction temperature at which 90% NH_3 conversion was achieved (T_{90}). ESI† shows the temperature dependence of the product selectivities for the combustion of NH_3 over the catalysts. For single catalysts supported on each material (*i.e.* 3A2S, Al_2O_3 and SiO_2), supported

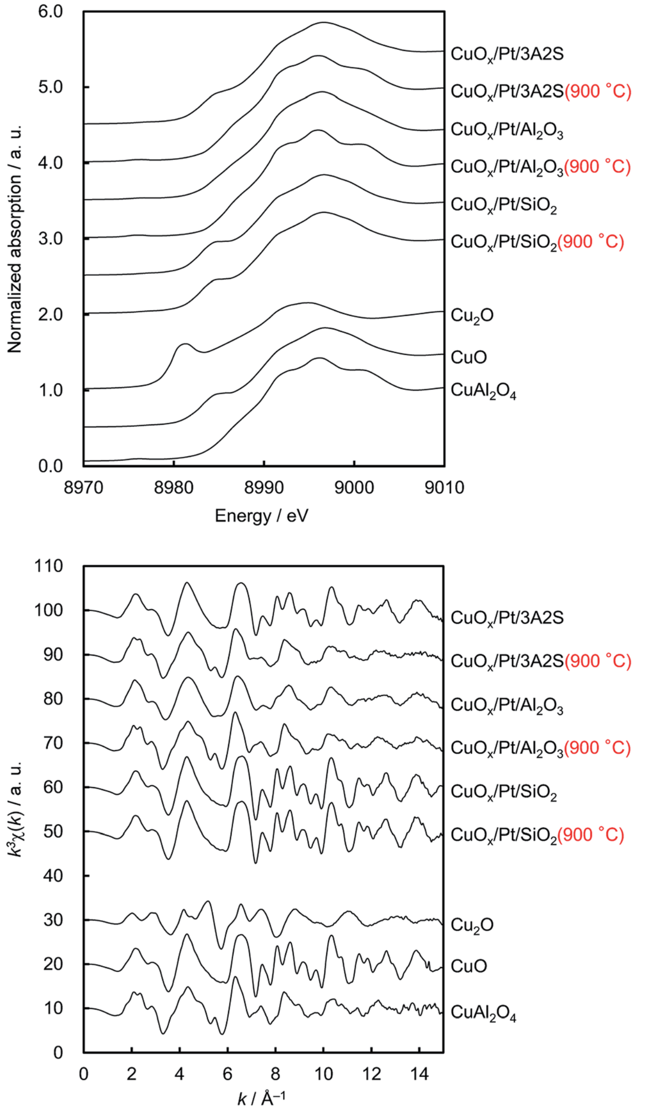

Fig. 2 Cu K-edge (upper) normalised XANES spectra and (lower) EXAFS oscillations of sequentially impregnated catalysts before and after thermal aging and three references (*i.e.* Cu_2O, CuO, and $CuAl_2O_4$, respectively).

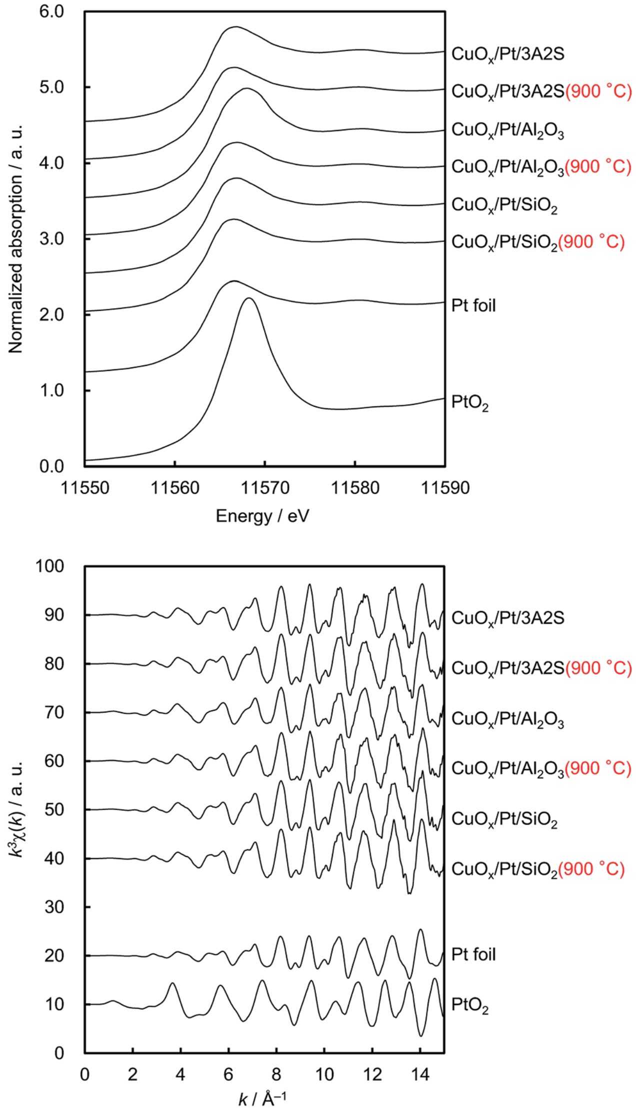

Fig. 3 Pt L_3-edge (upper) normalised XANES spectra and (lower) EXAFS oscillations of sequentially impregnated catalysts before and after thermal aging and two references (*i.e.* Pt foil and PtO_2, respectively).

CuO_x exhibited low activity and N_2O/NO selectivities, whereas supported Pt exhibited high activity and N_2O/NO selectivity (ESI†). On the other hand, binary supported catalysts exhibited the same high activity as the single supported Pt, albeit a slightly lower N_2O/NO selectivity. As the combustion activity was closely associated with the Pt particle size, which was calculated by the Scherrer equation (plot shown in the ESI†), highly dispersed Pt nanoparticles supposedly played a key role in the low-temperature light-off of NH_3. In this study, for pulsed CO chemisorption, it is expected that CO is adsorbed not only on Pt but also on CuO_x in case of binary system catalysts.[16] Therefore, the correlation between the NH_3 combustion activity (T_{10}) and the Pt particle size can be estimated using the XRD line broadening method by employing the Scherrer equation.

To elucidate the correlation between the activity and size of Pt nanoparticles, the adsorption energy (E_{ads}) between NH_3 and Pt_{13} and/or Pt_{20} clusters (Pt–N) were estimated by DFT computations (Fig. 7). Compared with the Pt–N E_{ads} of the vertex for the Pt_{20} (larger) cluster, that of the vertex for the Pt_{13} (smaller) cluster was higher, indicating that NH_3 preferentially adsorbs on highly dispersed Pt nanoparticles as well as coordinatively unsaturated (cus) Pt atoms. Indeed, for the Pt_{20} cluster, the Pt–N E_{ads} of three initial geometries (see inset in Fig. 7) increased in the order of atop < edge < vertex. Moreover, the bond distance of N–H in NH_3 adsorbed on Pt_{13} was longer than that on Pt_{20}, suggesting that cus Pt exhibits high activity for the dissociation of the N–H bond in adsorbed NH_3. Compared with the activity of binary CuO_x–Pt catalysts prepared by co-impregnation, those of the sequentially impregnated CuO_x/Pt catalysts were higher

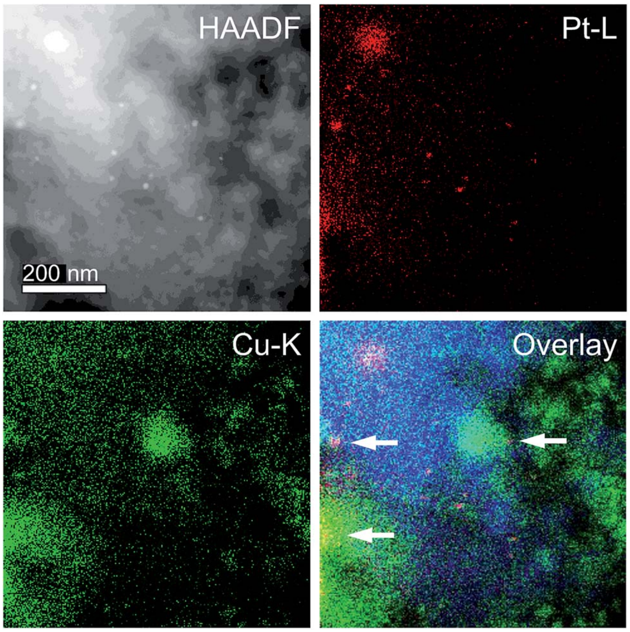

Fig. 4 HAADF-STEM image and EDS mapping analysis of $CuO_x/Pt/Al_2O_3$ (900 °C). Red, green, and blue points denote the Pt-L, Cu-K, and Al-K fluorescence lines, respectively.

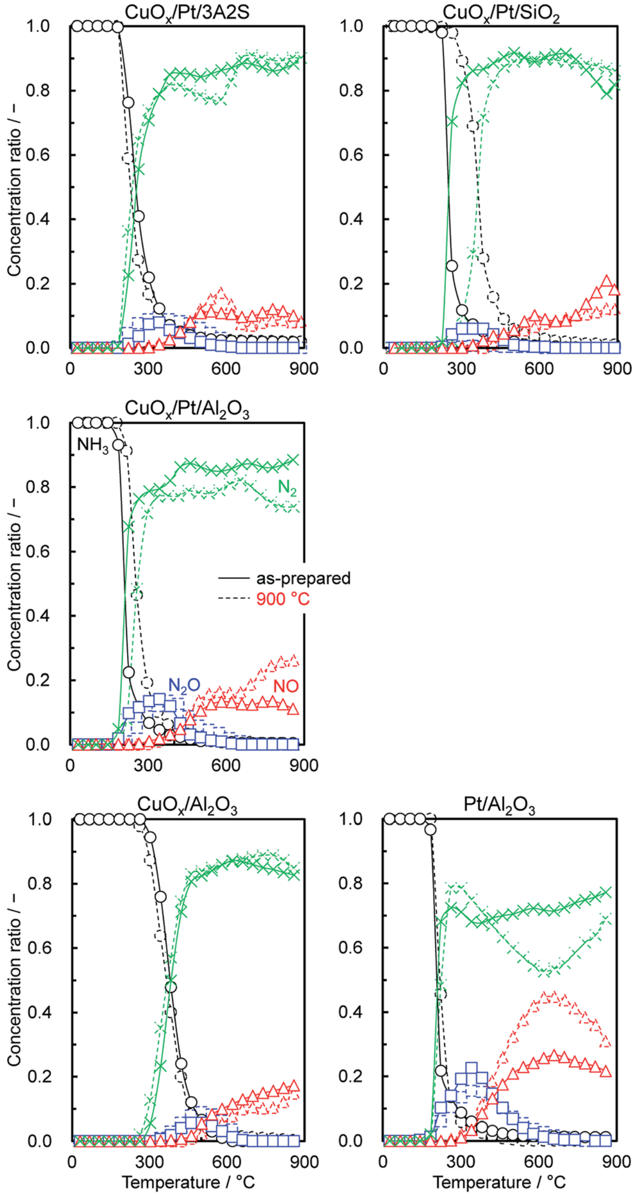

Fig. 5 Product selectivities for the catalytic combustion of NH_3 (NH_3–O_2) over catalysts before and after thermal aging in air at 900 °C for 100 h. Reaction conditions: 1.0% NH_3, 1.5% O_2, $\lambda = 2$, He balance, $W/F = 5.0 \times 10^{-4}$ g min cm^{-3}.

probably because Pt nanoparticles can be highly dispersed onto each support material without inhibition from the presence of CuO_x.

Among the CuO_x/Pt catalysts supported on various support materials, $CuO_x/Pt/Al_2O_3$ exhibited a relatively higher activity, N_2 selectivity, and thermal stability (Table 1). However, a significant decrease in S_{BET} was observed for $CuO_x/Pt/Al_2O_3$ (900 °C) (139 → 14 m^2 g^{-1}) in comparison with that observed for CuO_x/Al_2O_3 (900 °C) and Pt/Al_2O_3 (900 °C). For this reason, first, it is considered that the significant decrease in specific surface area can be attributed to the phase transition of ($\gamma \rightarrow \alpha$) Al_2O_3 as well as thermal aging at 900 °C. However, in case of only γ-Al_2O_3, the phase transformation to α-Al_2O_3 was observed at approximately 1200 °C.[17] Next, however, according to a previous report related to the effects of divalent cation additives on the phase transition of ($\gamma \rightarrow \alpha$) Al_2O_3, the additive Cu^{2+} species that coexist with γ-Al_2O_3 accelerates its phase transition to α-Al_2O_3 at a low temperature of 1200 °C, which can be attributed to the fact that $CuAl_2O_4$ is formed at a temperature of lower than 1200 °C.[18] Indeed, in this study, α-Al_2O_3 was observed in CuO_x/Al_2O_3 after thermal aging at 900 °C (Table 1). Finally, it is probable that the additive and co-existing Pt also accelerates the formation of $CuAl_2O_4$ as well as the phase transition to α-Al_2O_3. Although no concrete data are available, a similar significant decrease of the specific surface area could be observed in both Cu–Al–O and Cu–Pt–Al–O system catalysts after thermal aging occurred at 1000 °C.[19]

Notably, the high performance for $CuO_x/Pt/Al_2O_3$ was maintained after thermal aging at 1000 °C despite the phase transition ($\gamma \rightarrow \alpha$) and decrease in the surface area. On the other hand, CuO_x/Pt supported on α-Al_2O_3 exhibited slightly higher N_2O/NO selectivities compared to $CuO_x/Pt/Al_2O_3$ (using γ-Al_2O_3), the results of which can be explained from the difference in the CuO_x phase of CuO in $CuO_x/Pt/\alpha$-Al_2O_3 and $CuAl_2O_4$ in $CuO_x/Pt/\gamma$-Al_2O_3. Previously, our group has reported that supported $CuAl_2O_4$ exhibits a higher NH_3–NO–O_2 reaction activity to N_2 compared to supported CuO because supported $CuAl_2O_4$ exhibits a higher fraction of the Cu^{2+} active species for the reaction.[4] Therefore, the trend for N_2O/NO selectivities over $CuO_x/Pt/\alpha$-Al_2O_3 and $CuO_x/Pt/Al_2O_3$ can be explained in a similar manner. Moreover, physically mixed catalysts (CuO + Pt/Al_2O_3, $CuAl_2O_4$ + Pt/Al_2O_3 and CuO_x/Al_2O_3 + Pt/Al_2O_3) exhibited lower N_2 selectivity at high reaction temperatures (*ca.* > 600 °C) compared to binary catalysts (ESI†), indicating that highly dispersed Pt and proximate CuO_x particles

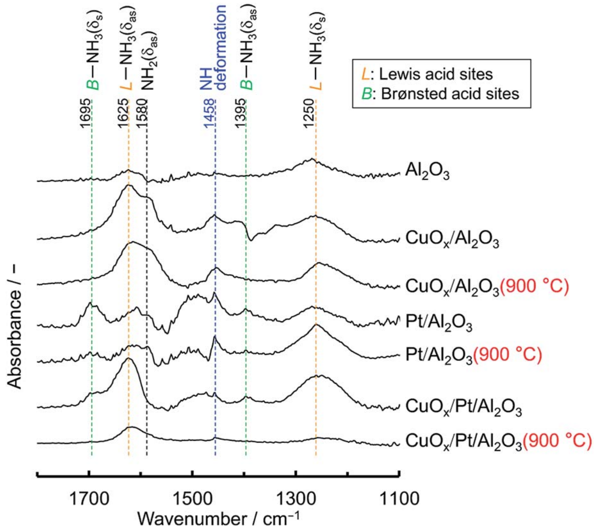

Fig. 6 *In situ* FTIR spectra of NH_3 adsorbed on supports and catalysts before and after thermal aging in air at 900 °C for 100 h. The spectra were recorded at 200 °C in gas feeds of 0.3% NH_3 with He balance.

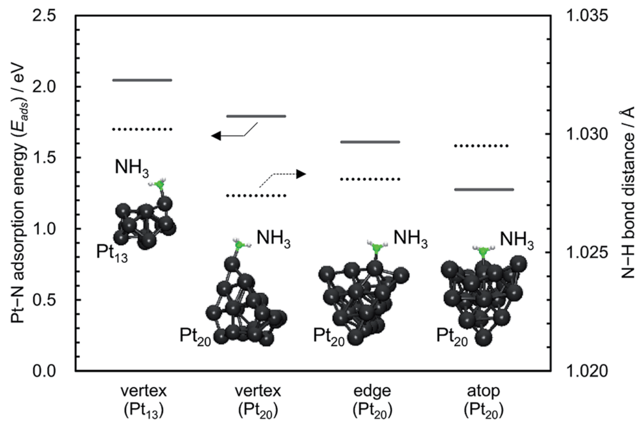

Fig. 7 Adsorption energy (E_{ads}) between NH_3 and Pt_{13} and/or Pt_{20} clusters (Pt–N) and bond distances of N–H in NH_3 adsorbed on Pt_{13} and/or Pt_{20} obtained by the DFT computations.

are required to achieve high N_2 selectivity for catalytic NH_3 combustion. On the other hand, Pt/CuO exhibited high N_2 selectivity, albeit low catalytic activity (ESI†), probably because of low Pt dispersion. To examine the acid and base properties of these catalysts, the amount of desorbed gas per surface area of the catalyst was estimated using NH_3- and NO-temperature-programmed desorption (TPD) over a range of 50–500 °C (ESI†). Table 1 summarises this data. For all catalysts after aging, the amount of desorbed NO increased noticeably, likely because of decreased surface area. However, before and after aging, CuO_x/Pt/Al_2O_3 exhibited relatively higher NH_3 and NO adsorption properties compared to CuO/Al_2O_3 and Pt/Al_2O_3. These results indicated that CuO_x/Pt/Al_2O_3 exhibits higher acidity and basicity compared to single supported catalysts; therefore, the reactivity of NH_3–NO to N_2 is enhanced on the CuO_x/Pt/Al_2O_3 surface.

Finally, the effects of CuO, Cu_2O and metallic Cu on the catalytic NH_3 combustion properties are discussed. ESI† denotes the comparison of the temperature dependence on the selectivities of the products that were obtained when compared to those of the commercially available CuO, Cu_2O and metallic Cu. The metallic Cu was prepared from CuO that was reduced at 400 °C for 30 min in 5% H_2/He because CuO can be reduced to metallic Cu at an approximate temperature of 300 °C, as demonstrated from the H_2-TPR measurement.[4] For observing the NH_3 combustion activity, the light-off curve for CuO was obtained at approximately 300 °C; further, Cu_2O and metallic Cu exhibited lower activity when compared to that exhibited by CuO. Therefore, it can be considered that CuO (Cu^{2+} oxidation state) acts as an active site during the reaction. However, while considering the selectivities of the products, Cu_2O and metallic Cu exhibited low N_2O/NO selectivities because their activities (NH_3 conversions) were observed to be low. In the O_2-excess condition for NH_3 combustion ($\lambda = 2.0$), it can be considered that the combustion over CuO_x catalysts proceeds because of redox cycling between CuO and Cu_2O.[4] Further, the XRD patterns of CuO and Cu_2O before and after the reaction ($\lambda = 2.0$) also indicate redox cycling because the patterns of Cu_2O after the reaction revealed diffraction peaks corresponding to those of CuO (ESI†). In addition, based on our previous studies related to *operando* XAFS, similar redox behaviours could be observed in the supported CuO catalysts (CuO_x/SiO_2).[4] Therefore, it can be assumed that the effect of metallic Cu on combustion is negligible.

Conclusions

In this study, binary CuO_x and Pt catalysts supported on 3A2S, Al_2O_3 and SiO_2 suppressed the production of N_2O/NO_x *via* the catalytic combustion of NH_3 as a carbon-free energy source. Among the binary supported CuO_x and Pt catalysts, sequentially impregnated CuO_x/Pt catalysts tended to exhibit higher activity because Pt nanoparticles were highly dispersed onto each support material without inhibition due to the presence of CuO_x. Compared to sequentially impregnated CuO_x/Pt/3A2S and CuO_x/Pt/SiO_2, CuO_x/Pt/Al_2O_3 exhibited high NH_3 combustion activity, N_2 selectivity, and thermal stability. Before and after aging, CuO_x/Pt/Al_2O_3 was characterised as proximate $CuAl_2O_4$ and dispersed metallic Pt particles. As the combustion activity was closely associated with the Pt particle size, highly dispersed Pt nanoparticles were thought to play a key role in the low-temperature light-off of NH_3. For selectivity, the proximate $CuAl_2O_4$ in CuO_x/Pt/Al_2O_3 enhanced the NH_3–NO to N_2 reaction, and the catalyst prevented the dissociative adsorption of NH_3 to NH, which was regarded as an intermediate species obtained during the N_2O production. Therefore, CuO_x/Pt/Al_2O_3 exhibits high N_2 selectivity.

Conflicts of interest

There are no conflicts to declare.

Acknowledgements

This research was supported by JST, PRESTO (JPMJPR1344) and JSPS (18K14326). This work was partly supported by JST-Mirai

Program and the Advanced Characterization Platform of the Nanotechnology Platform Japan sponsored by the Ministry of Education, Culture, Sports, Science and Technology (MEXT), Japan. The XAFS experiments were performed at BL9A with the approval of PF, KEK (Proposal No. 2016G527), and at the BL01B1 of SPring-8 with the approval of JASRI (Proposal No. 2017A1050).

Notes and references

1 P. Glarborg, A. Jensen and J. Johnsson, *Prog. Energy Combust. Sci.*, 2003, **29**, 89–113.

2 (*a*) J. Andersson and J. Lundgren, *Appl. Energy*, 2014, **130**, 484–490; (*b*) Y. Bicer, I. Dincer, C. Zamfirescu, G. Vezina and F. Raso, *J. Cleaner Prod.*, 2016, **135**, 1379–1395; (*c*) S. Giddey, S. Badwal, C. Munnings and M. Dolan, *ACS Sustainable Chem. Eng.*, 2017, **5**, 10231–10239.

3 (*a*) A. Hayakawa, T. Goto, R. Mimoto, T. Kudo and H. Kobayashi, *Mech. Eng. J.*, 2015, **2**, 14–00402; (*b*) R. Murai, R. Omori, R. Kano, Y. Tada, H. Higashino, N. Nakatsuka, J. Hayashi, F. Akamatsu, K. Iino and Y. Yamamoto, *Energy Procedia*, 2017, **120**, 325–332.

4 (*a*) S. Hinokuma, *et al.*, *Chem. Lett.*, 2016, **45**, 179–181; (*b*) S. Hinokuma, *et al.*, *J. Phys. Chem. C*, 2016, **120**, 24734–24742; (*c*) S. Hinokuma, *et al.*, *J. Phys. Chem. C*, 2017, **121**, 4188–4196; (*d*) S. Hinokuma, *et al.*, *J. Ceram. Soc. Jpn.*, 2017, **125**, 770–772; (*e*) S. Hinokuma, *et al.*, *Catal. Commun.*, 2018, **105**, 48–51; (*f*) S. Hinokuma, *et al.*, *Catal. Today*, 2018, **303**, 2–7; (*g*) S. Hinokuma, *et al.*, *J. Catal.*, 2018, **361**, 267–277.

5 (*a*) L. Gang, B. Anderson, J. van Grondelle, R. van Santen, W. van Gennip, J. Niemantsverdriet, P. Kooyman, A. Knoester and H. Brongersma, *J. Catal.*, 2002, **206**, 60–70; (*b*) M. Yang, C. Wu, C. Zhang and H. He, *Catal. Today*, 2004, **90**, 263–267; (*c*) J. Lee, Y. Lim, B. Park, A. Adelodun and Y. Jo, *Bull. Korean Chem. Soc.*, 2015, **36**, 162–167.

6 (*a*) R. Burch and B. Southward, *J. Catal.*, 2000, **195**, 217–226; (*b*) R. Burch and B. Southward, *Chem. Commun.*, 2000, 1115–1116; (*c*) H. Kusar, A. Ersson, M. Vosecky and S. Jaras, *Appl. Catal., B*, 2005, **58**, 25–32; (*d*) G. Olofsson, A. Hinz and A. Andersson, *Chem. Eng. Sci.*, 2004, **59**, 4113–4123; (*e*) G. Olofsson, L. Wallenberg and A. Andersson, *J. Catal.*, 2005, **230**, 1–13; (*f*) M. Sun, S. Wang, Y. Li, Q. Wang, H. Xu and Y. Chen, *J. Taiwan Inst. Chem. Eng.*, 2017, **78**, 401–408; (*g*) M. Jabłońska, *Catal. Commun.*, 2015, **70**, 66–71.

7 S. Lin, A. Gluhoi and B. Nieuwenhuys, *Catal. Today*, 2004, **90**, 3–14.

8 M. Lippits, A. Gluhoi and B. Nieuwenhuys, *Catal. Today*, 2008, **137**, 446–452.

9 H. Suzuki, M. Shimizu, H. Kamiya, T. Ota and M. Takahashi, *Adv. Powder Technol.*, 1997, **8**, 311–323.

10 B. D. Cullity, *Elements of X-RAY DIFFRACTION*, Addison-Wesley Publishing Company, Inc., Philippines, 1978.

11 (*a*) M. Hatanaka, N. Takahashi, T. Tanabe, Y. Nagai, A. Suda and H. Shinjoh, *J. Catal.*, 2009, **266**, 182–190; (*b*) J. Anderson, R. Daley, S. Christou and A. Efstathiou, *Appl. Catal., B*, 2006, **64**, 189–200; (*c*) Y. Nagai, T. Hirabayashi, K. Dohmae, N. Takagi, T. Minami, H. Shinjoh and S. Matsumoto, *J. Catal.*, 2006, **242**, 103–109.

12 (*a*) Y. Zhao and D. G. Truhlar, *Theor. Chem. Acc.*, 2008, **120**, 215–241; (*b*) A. Schäfer, H. Horn and R. Ahlrichs, *J. Chem. Phys.*, 1992, **97**, 2571–2577; (*c*) D. Andrae, U. Häussermann, M. Dolg, H. Stoll and H. Preuss, *Theor. Chim. Acta*, 1990, **77**, 123–141; (*d*) R. Ahlrichs, M. Bär, M. Häser, H. Horn and C. Kölmel, *Chem. Phys. Lett.*, 1989, **162**, 165–169; (*e*) TURBOMOLE, A development of University of Karlsruhe and Forschungszentrum Karlsruhe GmbH, 1989-2007, TURBOMOLE GmbH, since 2007, available from http://www.turbomole.com; (*f*) K. Eichkorn, F. Weigend, O. Treutler and R. Ahlrichs, *Theor. Chem. Acc.*, 1997, **97**, 119–124.

13 (*a*) F. Giordanino, E. Borfecchia, K. Lomachenko, A. Lazzarini, G. Agostini, E. Gallo, A. Soldatov, P. Beato, S. Bordiga and C. Lamberti, *J. Phys. Chem. Lett.*, 2014, **5**, 1552–1559; (*b*) U. Deka, A. Juhin, E. Eilertsen, H. Emerich, M. Green, S. Korhonen, B. Weckhuysen and A. Beale, *J. Phys. Chem. C*, 2012, **116**, 4809–4818.

14 Z. Tian, Y. Li, L. Zhang, P. Glarborg and F. Qi, *Combust. Flame*, 2009, **156**, 1413–1426.

15 (*a*) S. Yang, Y. Liao, S. Xiong, F. Qi, H. Dang, X. Xiao and J. Li, *J. Phys. Chem. C*, 2014, **118**, 21500–21508; (*b*) Y. Liu, T. Gu, X. Weng, Y. Wang, Z. Wu and H. Wang, *J. Phys. Chem. C*, 2012, **116**, 16582–16592; (*c*) L. Darvell, K. Heiskanen, J. Jones, A. Ross, P. Simell and A. Williams, *Catal. Today*, 2003, **81**, 681–692; (*d*) G. Busca, L. Lietti, G. Ramis and F. Berti, *Appl. Catal., B*, 1998, **18**, 1–36; (*e*) J. Amores, V. Escribano, G. Ramis and G. Busca, *Appl. Catal., B*, 1997, **13**, 45–58; (*f*) G. Ramis, L. Yi, G. Busca, M. Turco, E. Kotur and R. Willey, *J. Catal.*, 1995, **157**, 523–535; (*g*) B. Duffy, H. Curryhyde, N. Cant and P. Nelson, *J. Catal.*, 1994, **149**, 11–22.

16 (*a*) V. Dasireddy, B. Likozar and J. Valand, *Appl. Catal., B*, 2018, **237**, 1044–1058; (*b*) S. Lambert, C. Cellier, P. Grange, J. Pirard and B. Heinrichs, *J. Catal.*, 2004, **221**, 335–346.

17 G. Busca, *Catal. Today*, 2014, **226**, 2–13.

18 K. Okada, A. Hattori, T. Taniguchi, A. Nukui and R. Das, *J. Am. Ceram. Soc.*, 2000, **83**, 928–932.

19 M. Ferrandon, B. Ferrand, E. Bjornbom, F. Klingstedt, A. Neyestanaki, H. Karhu and I. Vayrynen, *J. Catal.*, 2001, **202**, 354–366.